

Scanning tunneling microscopy and spectroscopy studies of the heavy-electron superconductor TiNi_2Se_2

Stefan Wilfert,^{1,*} Martin Schmitt,^{1,†} Henrik Schmidt,¹ Tobias Mauerer,¹ Paolo Sessi,¹ Hangdong Wang,^{2,3} Qianhui Mao,² Minghu Fang,^{2,4} and Matthias Bode^{1,5}

¹Physikalisches Institut, Experimentelle Physik II, Universität Würzburg, Am Hubland, D-97074 Würzburg, Germany

²Department of Physics, Zhejiang University, Hangzhou 310027, China

³Department of Physics, Hangzhou Normal University, Hangzhou 310036, China

⁴Collaborative Innovation Center of Advanced Microstructures, Nanjing 210093, China

⁵Wilhelm Conrad Röntgen-Center for Complex Material Systems (RCCM), Universität Würzburg, Am Hubland, D-97074 Würzburg, Germany



(Received 3 July 2017; published 19 January 2018)

We report on the structural and superconducting electronic properties of the heavy-electron superconductor TiNi_2Se_2 . By using a variable-temperature scanning tunneling microscopy (VT-STM) the coexistence of $(\sqrt{2} \times \sqrt{2})\text{R}45^\circ$ and (2×1) surface reconstructions is observed. Similar to earlier observations on the “122” family of Fe-based superconductors, we find that their respective surface fraction strongly depends on the temperature during cleavage, the measurement temperature, and the sample’s history. Cleaving at low temperature predominantly results in the $(\sqrt{2} \times \sqrt{2})\text{R}45^\circ$ -reconstructed surface. A detailed analysis of the $(\sqrt{2} \times \sqrt{2})\text{R}45^\circ$ -reconstructed domains identifies (2×1) -ordered dimers, trimers, and higher order even multimers as domain walls. Higher cleaving temperatures and the warming of low-temperature-cleaved samples increases the relative weight of the (2×1) surface reconstruction. By slowly increasing the sample temperature T_s inside the VT-STM we find that the $(\sqrt{2} \times \sqrt{2})\text{R}45^\circ$ surface reconstructions transforms into the (2×1) structure at $T_s = 123$ K. We identify the polar nature of the $\text{TiNi}_2\text{Se}_2(001)$ surface as the most probable driving mechanism of the two reconstructions, as both lead to a charge density $\rho = 0.5 e^-$, thereby avoiding divergent electrostatic potentials and the resulting “polar catastrophe.” Low-temperature scanning tunneling spectroscopy (STS) performed with normal metal and superconducting probe tips shows a superconducting gap which is best fit with an isotropic s wave. We could not detect any correlation between the local surface reconstruction, suggesting that the superconductivity is predominantly governed by TiNi_2Se_2 bulk properties. Correspondingly, temperature- and field-dependent data reveal that both the critical temperature and critical magnetic field are in good agreement with bulk values obtained earlier from transport measurements. In the superconducting state the formation of an Abrikosov lattice is observed without any zero bias anomaly at the vortex core.

DOI: 10.1103/PhysRevB.97.014514

I. INTRODUCTION

It is probably fair to say that high-temperature superconductivity belongs to the remaining mysteries of solid-state physics. Since its discovery in cuprates in 1986 [1], physicists have (yet unsuccessfully) attempted to develop a unifying theory that explains the origin of superconductivity in this material class. In this context, the discovery of Fe-based pnictides [2,3] with bulk critical temperatures up to 55 K [4], or of the related, weaker correlated “122” systems represented a very significant finding as it demonstrated that high-temperature superconductivity was not limited to cuprates but could also be found in other materials [5].

In recent years, Fe- or Ni-based “122” systems were intensively investigated. The presence of Fe or Ni in these superconducting compounds led to speculations about the fundamental pairing mechanism of unconventional superconductivity because magnetism and superconductivity are

generally considered to be mutually exclusive [6]. Whereas the Fe chalcogenides $A_x\text{Fe}_{2-y}\text{Se}_2$ (A represents the elements Tl, K, Cs, or Pb) are inhomogeneous superconductors, Ni-based chalcogenides are stoichiometric, as verified by x-ray spectroscopy [7]. Furthermore, the Fermi surface of “122” superconductors exhibits no hole pockets, such that an electron-hole quasinegating coupling mechanism, which is characteristic for Cooper pair formation in Fe-based pnictides, can safely be excluded.

In 2013 superconductivity was discovered in TiNi_2Se_2 [7]. The bulk critical temperature of this compound amounts to $T_C^{\text{bulk}} = 3.7$ K only, i.e., much lower than the corresponding values of cuprates or even Fe-based superconductors. Furthermore, a moderate critical field $H_C^{\text{bulk}} \approx 0.6$ T (at $T = 1.2$ K) and—given the relatively weak correlation effects—a surprisingly large Sommerfeld coefficient were found. Detailed temperature- and field-dependent measurements of the electronic specific heat showed some interesting features, as they indicated a d -electron system with a very high effective mass $m^* = (17 \pm 3)m_e$, placing TiNi_2Se_2 somewhere “between cuprate- or iron-based and conventional heavy-fermion superconductors” [7].

*Corresponding author: swilfert@physik.uni-wuerzburg.de

†Corresponding author: maschmitt@physik.uni-wuerzburg.de

In the meantime several experimental and theoretical techniques have been employed to better understand the particular electronic properties that lead to superconductivity in TiNi_2Se_2 [8–10]. Measurements of the thermal conductivity κ_0 and specific heat γ_0 of TiNi_2Se_2 and the related compounds $\text{TiNi}_2\text{Se}_{(2-x)}\text{S}_x$ and CsNi_2Se_2 showed a very low residual electronic contribution, which is rather unlikely for nodal quasiparticles but instead indicates node-less superconductivity [8,9,11]. Furthermore, field-dependent data of κ_0 resembled similar data on NbSe_2 and were interpreted as evidence for the existence of at least two gaps with a ratio $\Delta_s/\Delta_1 \approx 0.6$. A detailed analysis allowed for the determination of the Ginzburg-Landau coherence length $\xi = 20$ nm [8]. Not surprisingly for a stoichiometric crystalline compound it was found that TiNi_2Se_2 is in the clean limit as its electron mean free path is one to two orders of magnitude larger than ξ [8]. Optical spectroscopy measurements showed that TiNi_2Se_2 is a good metal with a distinct plasma reflectance [9]. The progressive formation of a pseudogap at $T \leq 300$ K was interpreted as evidence for fluctuating charge density waves (CDW) which possibly eventually order at low temperatures [9].

These bulk-sensitive studies were complemented by a more surface sensitive angle-resolved photoemission (ARPES) study [10]. Photon energy-dependent data showed a three-dimensional band structure of TiNi_2Se_2 with four bands crossing the Fermi level. These γ bands exhibit asymmetric back-bending which results in a “camelback”-shaped feature near the Z point of the surface Brillouin zone (SBZ). As a result four small, partially overlapping lobes are formed, the flat parts of which give rise to a van Hove singularity. It was speculated that this shape of the Fermi surface is responsible for the unusually high Sommerfeld coefficient of TiNi_2Se_2 [10].

Further surface studies of Ni-based “122” systems would be highly interesting, in particular given recent results obtained on the mixed-valence–driven heavy-fermion superconductors KNi_2Se_2 and KNi_2S_2 [12,13]. These bulk-sensitive experiments were interpreted in terms of electronically driven phase transitions where the hybridization of delocalized electrons with charge-ordered states severely impacts the formation of heavy-electron states and superconductivity. Since (001) surfaces of “122” superconductors often display charge-driven reconstructions [14–20], it is not at all clear how superconductivity of TiNi_2Se_2 would react to their presence. Contradictory results have been published for other “122” materials, covering the entire range from very significant reconstruction-induced variations of the local superconducting properties [14,18] to their complete absence [16].

Here we present a scanning tunneling microscopy (STM) and spectroscopy (STS) study of the structural and electronic properties of TiNi_2Se_2 . We performed temperature- and magnetic field-dependent measurements on (001) surfaces that were prepared by cleaving the bulk material *in situ* under ultrahigh vacuum conditions. Topographic data reveal that surfaces created by cleaving at low temperature are dominated by a $(\sqrt{2} \times \sqrt{2})\text{R}45^\circ$ structure with occasional $\langle 100 \rangle$ -oriented straight stripes. These reconstructions lead to a surface charge density of $\rho < 0.5 e^-$ per unit cell which is required to avoid a polar catastrophe due to the polar character of the $\text{TiNi}_2\text{Se}_2(001)$ planes. With increasing cleaving temperature the stripes cover a larger and larger surface fraction. Heating to

temperature $T \geq 126$ K or room temperature cleaving results in a “wormlike” structure with more irregular and shorter stripe segments. We show that the stripes are caused by Ti multimers which form (1×2) -reconstructed domain walls between adjacent $(\sqrt{2} \times \sqrt{2})\text{R}45^\circ$ domains if they consist of an even number of Ti atoms, i.e., for dimers, tetramers, etc. STS measurements performed at $T = 1.2$ K show a V-shaped gap which appears to be uncorrelated with the local surface reconstruction, suggesting that the superconductivity is predominantly governed by TiNi_2Se_2 bulk properties rather than surface’s structural and charge-ordered state. Temperature- and field-dependent STS data result in a surface Curie temperature $T_C^{\text{surf}} = 3.05$ K and a critical field $\mu_0 H_C^{\text{surf}} = 0.35$ T, in reasonable agreement with the bulk data determined previously [7]. Finally, we show that the application of an external magnetic field produces an Abrikosov lattice of magnetic flux quanta typical for type II superconductors.

II. EXPERIMENTAL PROCEDURES

The TiNi_2Se_2 single crystals were grown by a self-flux method. Stoichiometric amounts of Ti, Ni, and Se were placed in a sealed alumina crucible, heated at 950°C for 12 h, and cooled to 700°C at a rate of 6°C/h, before further cooling (see Ref. [7] for details). The resulting single crystals were cut with a scalpel to pieces suitably sized for STM measurements.

Scanning tunneling microscopy (STM) and spectroscopy (STS) experiments were carried out with three scanning tunneling microscopes, each covering a dedicated temperature range. A commercial variable-temperature scanning tunneling microscope (VT-STM) operates at sample temperatures $40\text{ K} \leq T_s \leq 400\text{ K}$, in a commercial low-temperature STM (LT-STM) with a base temperature of 4.8 K the sample temperature can be raised up to $T_s \approx 20$ K, and a home-built cryogenic STM (1K-STM) with minimal temperature $T_s = 1.2$ K, which can be operated up to $T_s \approx 10$ K, is dedicated for measurements of the superconducting properties. The latter is also equipped with a superconducting solenoid coil that produces a magnetic field $|B| \leq 12.5$ T along the sample surface normal. All topographic images were obtained in the constant-current mode with electrochemically etched W tips. The bias voltage U is denoted such that positive (negative) values represent an electron tunnel current I which flows from occupied tip (sample) states into empty sample (tip) states. Spectroscopic data were recorded under open feedback loop conditions by adding a small modulation voltage U_{mod} to the bias voltage U (frequency $f = 876.5$ Hz) and measuring the resulting differential conductance dI/dU by means of a lock-in amplifier. The differential conductance dI/dU maps showing the Abrikosov lattice were also obtained by means of a lock-in but with the feedback loop closed.

For optimal surface quality we cleave the single crystals *in situ* under UHV conditions (pressure $p \leq 1 \times 10^{-9}$ mbar). As will be described in detail below we found that the cleaving temperatures T_{cleave} have important consequences for the surface morphology of TiNi_2Se_2 . Since the experimental setups of the three STMs used for this study slightly vary, also the respective values for T_{cleave} and the procedures differ substantially. In the VT- and the LT-STM we use special sample

holders which allows one to first insert the sample into the STM sample slot where it cools down to the targeted temperature before being cleaved *within* the STM, i.e., without taking the sample out of the STM sample slot. Thereby, we achieve values between $50 \text{ K} \leq T_{\text{cleave}} \leq 300 \text{ K}$ for the VT-STM and $T_{\text{cleave}} \leq 5 \text{ K}$ for the LT-STM. Unfortunately, due to its relatively large size it was not possible to use the same sample holder in the 1K-STM. In the 1K-STM UHV system, the sample was cleaved in a storage slot mounted inside the LHe shield. Whereas the temperature within this storage slot is probably very close to 5 K, it had to be transferred into the STM with an uncooled manipulator. Although we cannot determine the maximum sample temperature during this transfer, the subsequently imaged surface always displayed what will be termed the “wormlike” structure below, indicative for reaching a sample temperature $T \geq 126 \text{ K}$.

III. RESULTS

A. Structural properties

Figure 1(a) shows the tetragonal crystal structure of TiNi_2Se_2 , which belongs to the ThCr_2Si_2 class with space group $I4/mmm$. The dimensions of the unit cell are $a = 3.870 \text{ \AA}$ in the (001) plane and $c = 13.435 \text{ \AA}$ along the [001] direction [7]. The layered structure consists of monovalent Ti^{1+} , bivalent Se^{2-} , and Ni atoms with a mixed valence of $\text{Ni}^{1.5+}$. Based on these valences, the Ni–Se bond strength is expected to be

stronger than for Ti–Se . Therefore, a cleavage process should result in (001) planes created by breaking the Ti–Se bonds either above or below the gray plane indicated in Fig. 1(a). Figure 1(b) shows the (001) surface of the TiNi_2Se_2 crystal structure in top view. The in-plane nearest neighbor distance in the Ti and Se layers equals the lattice constant a , whereas the lattice of the Ni layer is rotated by 45° and exhibits a Ni–Ni distance of $a/\sqrt{2} = 2.74 \text{ \AA}$.

Because the atomic environment is mirror symmetric with respect to this Ti plane, one would naively expect that upon cleavage half of the Ti atoms reside at the upper and the other half at the lower fragment, thereby preserving an uncharged configuration. The same result is obtained when considering the polar character of the $\text{TiNi}_2\text{Se}_2(001)$ surface. In fact, the above-mentioned valences lead to a Ni_2Se_2 block which is not neutral but carries a net charge of -1 . The corresponding positive charge $+1$ is located in the Ti layer. Let’s assume for a moment a cleavage process resulted in two fragments with different Ti surface densities. This would lead to two charged surfaces which carry a charge density $\rho < 0.5 e^-$ ($\rho > 0.5 e^-$) per unit cell on the side with the lower (higher) Ti surface concentration. Similar to the situation at a $\text{LaAlO}_3/\text{SrTiO}_3$ interface this would lead to the build-up of a divergent electrostatic potential and result in what was termed the “polar catastrophe” [21]. Therefore, any structure with a Ti surface density other than 0.5 atoms per unit cell is expected to be energetically unfavorable.

A material class that belongs to the same space group as our TiNi_2Se_2 crystals are the (001) surfaces of the so-called “122” Fe-based pnictide superconductors which have been intensively studied both theoretically and experimentally by STM [14–20]. Calculations of ternary iron arsenides with the composition $B\text{Fe}_2\text{As}_2$ ($B = \text{Ba}, \text{Sr}, \text{or Ca}$) predict a B -terminated surface [17]. $(\sqrt{2} \times \sqrt{2})$ - or (2×1) -reconstructed surfaces were found to be energetically favorable as compared to the unreconstructed (1×1) surface, but the energy difference between these reconstructed surfaces is often small [17]. Indeed, the coexistence of both structures was observed by STM for pure and lightly doped SrFe_2As_2 [14,19] and for lightly doped BaFe_2As_2 [15,18,20]. Although a dependence of the surface structure on the cleavage temperature has been discussed in several contributions, no consensus could be reached, as some studies find that the reconstructions are largely temperature independent [22,23] whereas others report on a substantial temperature dependence [16,19].

Figure 1(c) shows a typical topographic STM image of the (001) surface of the Ni-based superconductor TiNi_2Se_2 created by cleaving a sample inside the LT-STM at $T \leq 10 \text{ K}$. As can be seen in the line section plotted in Fig. 1(d) [drawn along the blue line in Fig. 1(c)] the surface exhibits atomically flat terraces which are separated by steps with a height of $(6.7 \pm 0.3) \text{ \AA}$, in agreement with the $c/2$ separation expected for adjacent Ti layers. The sketch in the lower left of Fig. 1(d) schematically visualizes the situation with the rectangular unit cell identical to the (010) plane of Fig. 1(a). Occasionally, we observe dark lines in our STM images, one of which is marked by a black arrow in Fig. 1(c). Their apparent depth typically amounts to about 1 \AA . We speculate that they represent dislocations that were either not fully annealed during crystal growth or

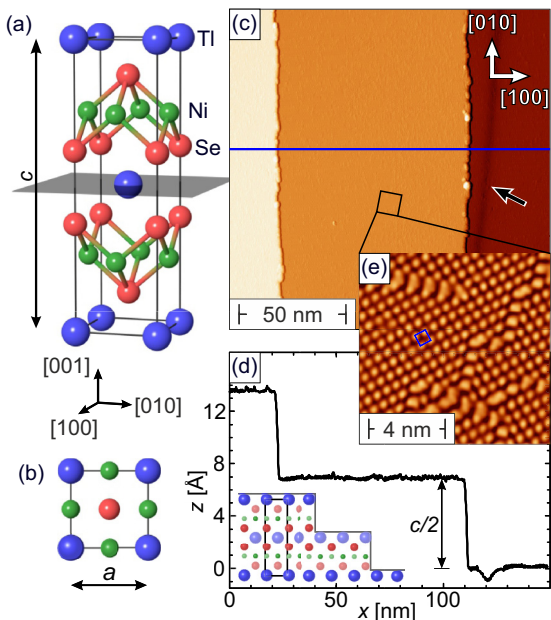


FIG. 1. (a) Crystal structure of TiNi_2Se_2 and probable cleavage plane (gray). (b) Top view illustrates a 45° rotation between nearest neighbor directions of Ti and Ni layers. (c) Topographic image with occasionally occurring dislocation lines (black arrow). The blue box of the $\sqrt{2} \times \sqrt{2}$ unit cell in the higher resolution image (e) is one of two typical structures for LT-cleaved samples. (d) Line section along the blue line in (c). The terraces are separated by step heights of the half-unit-cell as visualized in the lower left sketch. Scan parameters are as follows: $U = 500/10 \text{ mV}$, $I = 10/250 \text{ pA}$, and $T_s = 5 \text{ K}$ for (c) and (e), respectively.

created during the cleaving process. A high resolution scan measured within the region marked by a black square in Fig. 1(c) on an atomically flat terrace of the low-temperature-cleaved sample is shown in Fig. 1(e). We recognize a square-shaped unit cell which is consistent with a $(\sqrt{2} \times \sqrt{2})R45^\circ$ superstructure (blue square) and will be discussed in detail below.

To study the temperature dependence of the $\text{TiNi}_2\text{Se}_2(001)$ surface structure we cleaved single crystals taken from the same batch within the STM at different temperatures T_{cleave} . Subsequently, the samples were measured at low temperatures ($T_{\text{meas}} \leq 50$ K). The results are summarized in Fig. 2 for three different temperatures. As can be seen in Fig. 2(a) a surface cleaved at 5 K is dominated by the $(\sqrt{2} \times \sqrt{2})R45^\circ$ superstructure. In addition to the square-shaped unit cell already presented in Fig. 1(e), short one-dimensional (1D) stripes can be recognized which are separated by a distance $2a$ and orientated along the two high symmetry directions [100] or [010]. These characteristics are fully consistent with

the (2×1) reconstructions previously observed for “122” Fe-based pnictide superconductors [14–20]. As already mentioned above these reconstructions are an unavoidable consequence of the polar character of the Tl-terminated $\text{TiNi}_2\text{Se}_2(001)$ surface which consists of Ni_2Se_2 blocks (net charge -1) and Tl layers ($+1$). Upon cleavage the polar catastrophe can only be avoided if each surface unit cell carries a net charge of $+0.5 e^-$, i.e., half of the Tl atoms must remain on the surface of either of the two fragments. However, the Tl atoms on the cleaved surfaces are not randomly distributed but exhibit well-ordered reconstructions even at cleavage temperatures as low as $T_{\text{meas}} \leq 5$ K [cf. Figs. 1(e) and 2(a)]. This observation could be explained, for example, if the Tl atoms were able to rearrange even without thermal excitations, e.g., due to the mechanical energy dissipated during the cleaving process. Alternatively, it would require a cleaving process which intrinsically takes place such that—as far as the $(\sqrt{2} \times \sqrt{2})R45^\circ$ superstructure is concerned—an atomic checkerboard pattern is generated. In any case, we would like to stress that both

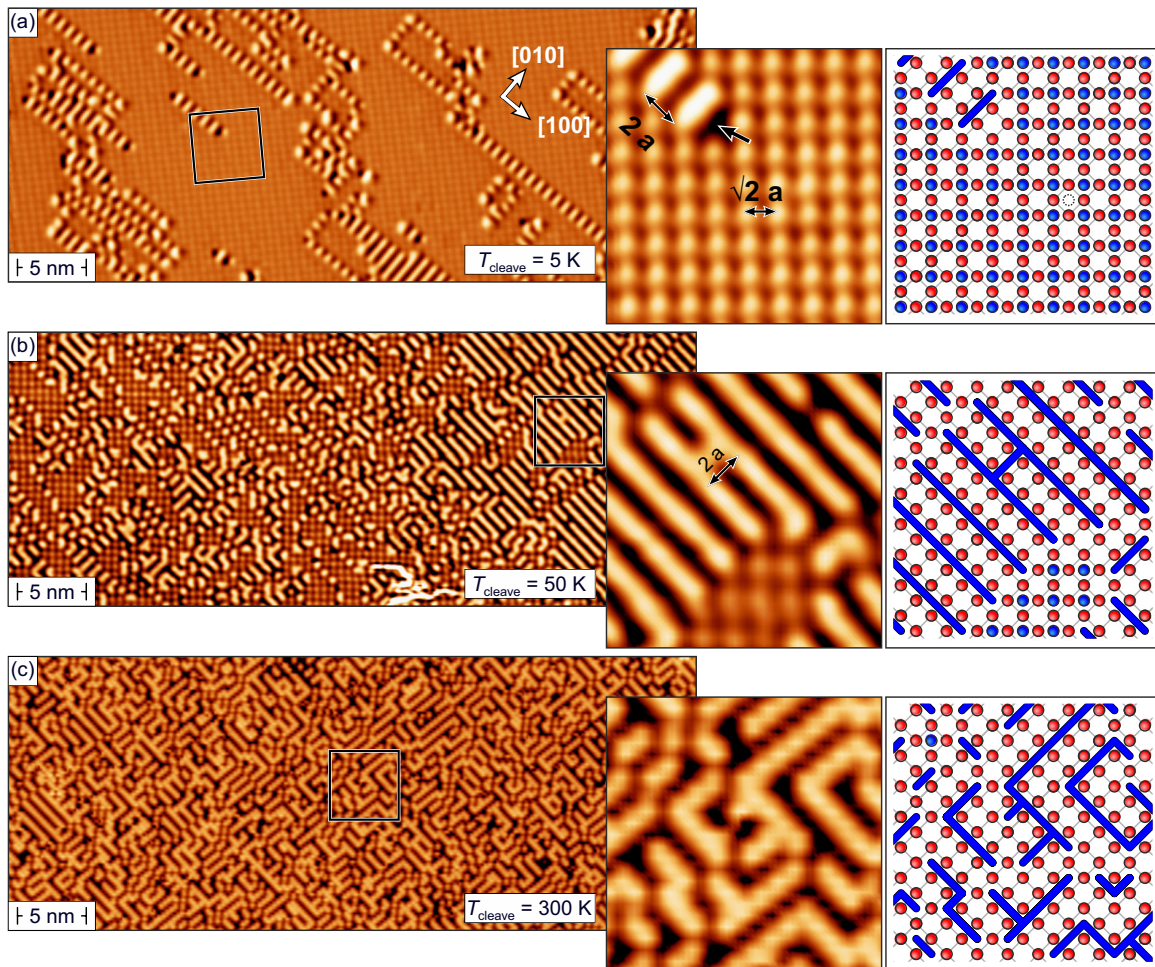


FIG. 2. Cleaving temperature dependence of the TiNi_2Se_2 surface structure. In either case an overview image (left panel), a zoom-in to the region within the black square (middle), and a model of the surface (right) are shown. Atoms of the topmost Se layer and the Tl cleavage plane are shown in red and blue, respectively. To highlight Tl atom rows, nearest-neighbor Tl atom with a Tl–Tl distance $a = 3.870$ Å are not resolved individually but as a continuous blue line. (a) If cleaved at 5 K the surface topography is dominated by large domains of a $(\sqrt{2} \times \sqrt{2})R45^\circ$ superstructure [imaging parameters (inset) are as follows: $U = 1(0.5)$ V, $I = 20(500)$ pA, $T_s = 5$ K]. (b) Cleavage at a temperature of 50 K lead to substantial stripes formation and smaller $(\sqrt{2} \times \sqrt{2})R45^\circ$ domains ($U = 50$ mV, $I = 20$ pA, $T_s = 50$ K). (c) A twofold symmetric “wormlike” structure is observed for room-temperature-cleaved TiNi_2Se_2 ($U = 1$ V, $I = 300$ pA, $T_s = 5$ K).

surface reconstructions, the $(\sqrt{2} \times \sqrt{2})R45^\circ$ as well as the (2×1) structure, result in the same surface charge of $+0.5 e^-$ per surface unit cell, thereby avoiding the polar catastrophe.

As shown in Fig. 2(b), an increased cleaving temperature $T_{\text{cleave}} = 50$ K yields essentially the same surface features, i.e., a $(\sqrt{2} \times \sqrt{2})R45^\circ$ square lattice and (2×1) reconstructed one-dimensional (1D) stripes, but at a different distribution between the two structures. In comparison to the sample surface presented in Fig. 2(a) which was cleaved at 5 K, the 1D stripes now cover a much larger fraction of the sample surface and at some places even form homogeneous domains which are as large as 20 nm in diameter. Consequently, the ratio of the $(\sqrt{2} \times \sqrt{2})R45^\circ$ square lattice, which still coexists with 1D stripes in the remaining regions of the surface, is reduced appropriately. It shall be mentioned that locally often one of the two possible high symmetry directions dominates, although both directions were found to be equally distributed in average, in agreement with the symmetry of the surface. The high-resolution STM image in the middle panel of Fig. 2(b) and the corresponding schematic model of the right panel visualize the arrangement of stripes and relate it to the (1×1) unit cell of TiNi_2Se_2 .

Finally, we cleaved a single crystal at $T_{\text{cleave}} = 300$ K. The surface structure of this sample always consists of short stripes which form a twofold symmetric “wormlike” structure [see left panel of Fig. 2(c)]. The high-resolution scan in the middle panel of Fig. 2(c) reveals a small modulation with a periodicity of (3.8 ± 0.3) Å along the stripes, which agrees well with the lattice constant of TiNi_2Se_2 . In spite of the fact that this surface in general still consists of the (2×1) stripe motif, this “wormlike” pattern is characterized by a strongly reduced stripe length [as compared to the situation presented in Fig. 2(b)] and by the coexistence of both stripe orientations even within a small surface area.

For the occurrence of the stripes mentioned above two possible scenarios are conceivable: (i) The stripes may be caused by domain boundaries that separate the two possible configurations of the $(\sqrt{2} \times \sqrt{2})R45^\circ$ reconstruction which differ by a lateral displacement a in either the $[100]$ or the $[010]$ direction. Alternatively, (ii) the stripes may also represent a (2×1) surface reconstruction which coexists and competes with the $(\sqrt{2} \times \sqrt{2})R45^\circ$ structure. If the latter explanation were correct, the fact that the (2×1) reconstruction covers a smaller fraction of the surface than the $(\sqrt{2} \times \sqrt{2})R45^\circ$ structure would indicate its somewhat higher total energy.

We can distinguish these two scenarios by a detailed analysis of the STM images shown in Figs. 3(a) and 3(b) which were both measured on TiNi_2Se_2 surfaces prepared by cleaving a single crystal at $T_{\text{cleave}} = 5$ K. In agreement with the data already presented in Fig. 2(a) the topography is dominated by several regions exhibiting a periodic $(\sqrt{2} \times \sqrt{2})R45^\circ$ square lattice. These $(\sqrt{2} \times \sqrt{2})R45^\circ$ -ordered regions are separated by boundaries consisting of stripes which are generally rather short but slightly differ in length. In the experimentally observed STM images of Figs. 3(a) and 3(b) we have marked four areas by black squares which are labeled with white numbers 1 through 4. The patterns observed within these regions are schematically presented in Fig. 3(c). The area labeled

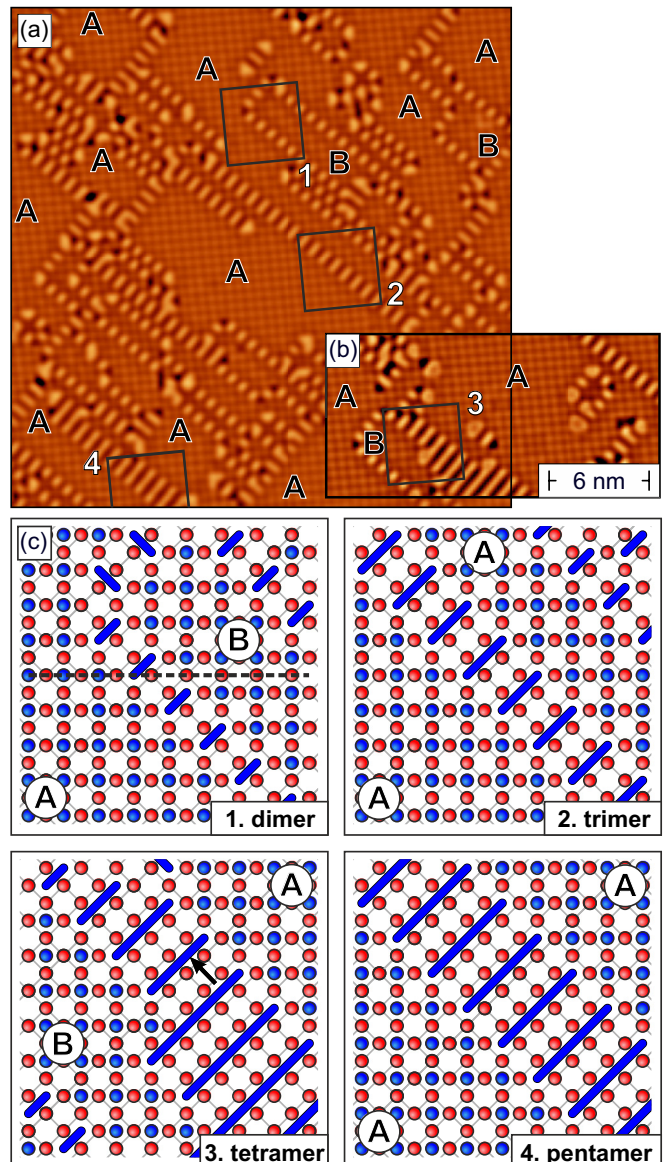


FIG. 3. (a) and (b) STM topographic images of TiNi_2Se_2 single crystal surfaces cleaved at $T_s = 5$ K. Scan parameters are as follows: $U = 1$ V, $I = 20$ pA. The surface is governed by $(\sqrt{2} \times \sqrt{2})R45^\circ$ -ordered patches labeled A or B, which are separated by boundaries that consist of short stripes. Four such regions marked by black squares and labeled 1–4 in panels (a) and (b) are schematically represented in (c). Analysis reveals that the stripes exhibit different length and represent dimers (1), trimers (2), tetramers (3), and pentamers (4). Whereas dimers and tetramers separate the inequivalent domains A and B, trimer and pentamer walls are always surrounded by the same domain.

1 displays two regions with a $(\sqrt{2} \times \sqrt{2})R45^\circ$ periodicity and relatively short stripes (length about 6 Å) in between. As indicated by a black hatched line, the Ti square lattice (blue dots) in the lower left region (labeled A) is shifted by one lattice constant a with respect to the one in the region in the upper right (B). This observation can only be explained if there is a structural domain boundary formed by a dimer that

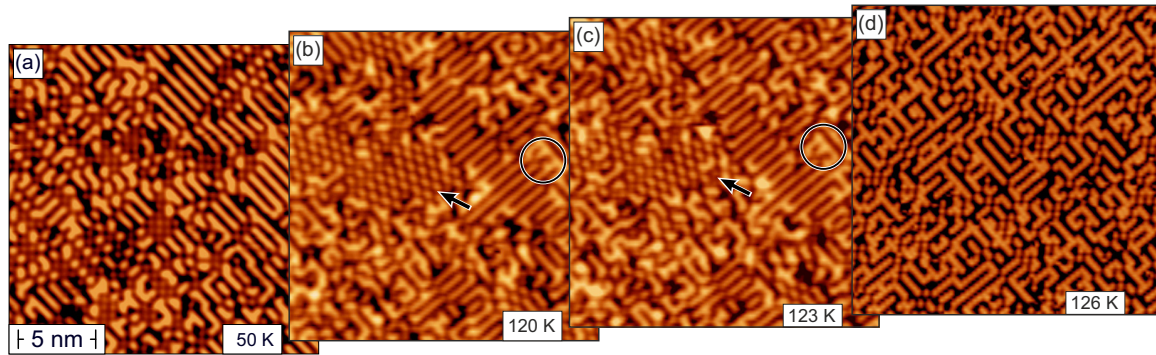


FIG. 4. (a) Both LT structures of TiNi_2Se_2 coexist on a sample cleaved at $T_{\text{cleave}} = 50$ K. This already changes at a temperature of $T_s = 120$ K in (b) where no square lattice is observed. By warming up to $T_s = 123$ K further changes are observed in (c). The transition into the “wormlike” structure in (d) is completed at $T = 126$ K. Circles serve as markers for same sample positions and black arrows for an example of restructuring. Scan parameters are as follows: $U = 50$ mV, $I = 20$ pA for (a) and $U = 1$ V, $I = 200\ldots 300$ pA for (b)–(d).

consists of two Tl atoms in nearest neighbor adsorption sites. In general agreement with this structural picture we also find longer stripes in Figs. 3(a) and 3(b) with a length of about 9 Å, 12 Å, and 16 Å (line sections not shown here) which we interpret as trimers (area 2), tetramers (3), and pentamers (4), respectively. Since the $(\sqrt{2} \times \sqrt{2})R45^\circ$ periodicity is translationally invariant when shifted by an equal multiple of the lattice constant a , only the dimer and the tetramer represent true domain walls as the trimer and pentamer walls are always surrounded by the same domain.

So far we found that depending on the actual cleaving temperature different surface structures can be observed on TiNi_2Se_2 . Furthermore, the detailed analysis of STM topography images taken at low temperatures revealed that the stripes which cover a small but significant portion of the sample surface are formed at domain walls where equivalent domains of the $(\sqrt{2} \times \sqrt{2})R45^\circ$ Tl surface lattice are offset by multiples of the lattice constant a . In the following, we want to discuss to what extent an already existing surface, which was originally cleaved at $T = 50$ K, changes as the temperature is raised. While the cooling process of room-temperature-cleaved samples was found to always result in a “wormlike” structure (not shown here), the warming process as investigated by VT-STM measurements is visualized in Fig. 4 for a sample which was initially cleaved within the STM at $T_{\text{cleave}} = 50$ K. Directly after the cleaving process the surface was imaged at $T_{\text{meas}} = 50$ K. As shown in Fig. 4(a) the surface structure is again characterized by (2×1) stripes that coexist with the $(\sqrt{2} \times \sqrt{2})R45^\circ$ square lattice, in agreement with the data presented in Fig. 2(b).

In the following the same sample was slowly heated at a rate of 1 K/min and imaged with the STM approximately every 5 K. No significant changes were observed for temperatures below 120 K. A drastically changed surface structure was, however, registered for Fig. 4(b) taken at $T_{\text{meas}} = 120$ K. Comparison with the low-temperature data of Fig. 4(a) reveals that the $(\sqrt{2} \times \sqrt{2})R45^\circ$ domain has vanished. As indicated by a black arrow in Fig. 4(b) it is replaced by short stripes orientated along the [100] direction. The length and orientation of the stripes is consistent with a periodic lattice of the Tl dimers discussed in Fig. 3. Within a few Kelvin this region rapidly transforms into a more complicated stripe pattern, as can be

recognized by comparing Figs. 4(b) and 4(c) which only differ by 3 K. When warming the sample a bit further to 126 K, the transition to this “wormlike” structure is completed [Fig. 4(d)]. Experiments not shown here indicate that the structure is irreversible as—by cooling—it can neither be transformed back to the $(\sqrt{2} \times \sqrt{2})R45^\circ$ nor to the regular (2×1) stripe phase.

Interestingly, all surface features reported here, i.e., the (2×1) -ordered stripes as well as the $(\sqrt{2} \times \sqrt{2})R45^\circ$ square cell, closely resemble what has been reported for pure and lightly alkaline-earth-doped Fe-based superconductors [14–16,18,19]. These materials possess the same crystal structure as TiNi_2Se_2 and cleave between As and alkaline planes such that the alkaline atoms are evenly divided between the two FeAs surfaces created by the cleaving process. While the Tl atoms form a regular $(\sqrt{2} \times \sqrt{2})R45^\circ$ surface structure with a few (2×1) -ordered domain walls when cleaved at low temperatures, our results show that heating to $T \geq 126$ K leads to an irreversible transition to a more irregular striped structure. This finding suggests that the $(\sqrt{2} \times \sqrt{2})R45^\circ$ superstructure is a metastable state. A similar cleavage temperature dependence of the surface structures has also been observed for Fe-based superconductors [16]. The irreversibility of the transition may be caused by Tl atoms which are not mobile enough to rearrange to full order at low temperatures, but possess sufficient energy for site changes in the temperature region around 126 K.

B. Electronic properties

1. Structure of the superconducting gap

Transport measurements have shown that TiNi_2Se_2 undergoes a superconducting phase transition at a critical temperature $T_C = 3.7$ K [7,8]. The observation of a very low residual electronic contribution to the thermal conductivity led to the conclusion of a node-less superconducting gap which is a common feature of Ni-based superconductors [8]. The STS spectrum of the superconducting gap structure of the very same TiNi_2Se_2 crystal used for the transport measurements in Ref. [7] is shown in Fig. 5. During the measurement the nominal tip and sample temperature was $T = 1.2$ K. The raw data were normalized to a constant background where the STS signal outside the superconducting gap serves as a reference.

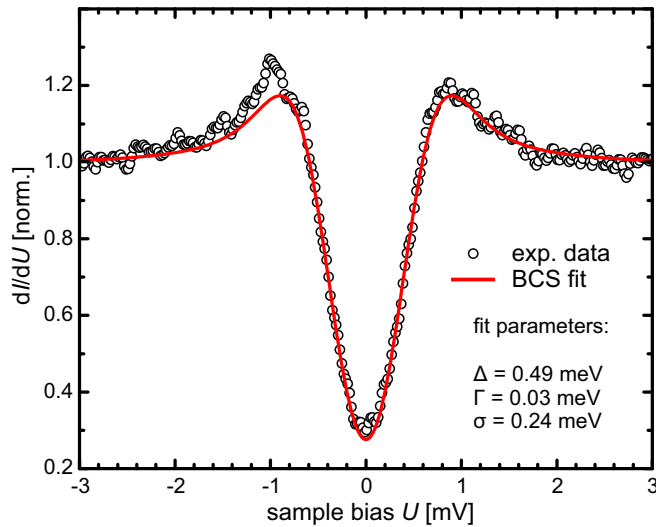


FIG. 5. STS signal of TiNi_2Se_2 recorded with a normal conducting W tip. The data are fitted by an isotropic [red, Eq. (1)]. Stabilization parameters are as follows: $U = -5$ mV, $I_{\text{set}} = 200$ pA, $U_{\text{mod}} = 0.1$ mV, $T = 1.2$ K.

A well-pronounced superconducting gap can be recognized. The gap seems to be V shaped and the STS dI/dU signal, which is essentially proportional to the local density of states at small bias voltages [24], does not vanish within the gap but only drops to about 30% of the value outside the gap. In order to determine whether this is an indication for an anisotropic gap function or the effect of a limited energy resolution, we fitted the data by a simple isotropic BCS-like gap function (red line in Fig. 5) [25],

$$\rho = \text{Re} \left[\frac{|E - i\Gamma|}{\sqrt{(E - i\Gamma)^2 + \Delta^2}} \right]. \quad (1)$$

Here E denotes the energy with respect to the Fermi level, with the Dynes parameter Γ [25]. The fit was broadened by the Fermi distribution, and a Gaussian broadening $\sigma = 0.24$ meV. Throughout this work, very similar values with $\Gamma = (0.04 \pm 0.01)$ meV and $\sigma = (0.28 \pm 0.04)$ meV were used for all spectra. Obviously, the isotropic BCS model fits our experimental data very well. As detailed in the Supplemental Material [26], however, similarly good fitting results are also obtained when assuming a gap with an anisotropic character. Therefore, we have to conclude that based on the available STS data it cannot be decided whether TiNi_2Se_2 exhibits an isotropic s wave or an anisotropic p -/ d -wave pairing mechanism.

2. Spatially resolved measurements

STM/STS measurements in principle allow one to spatially resolve on the atomic scale if and to what extent the superconducting gap depends on the surface location. It would be particularly interesting to investigate if the reconstructions observed by STM in Sec. III A of this paper have any influence on the superconducting gap. For example, in the related sample systems KNi_2Se_2 [12] and KNi_2S_2 [13] a close correlation between the low-temperature superconducting state and cooperative phenomena arising from Coulomb interactions and proximity to charge order have been observed.

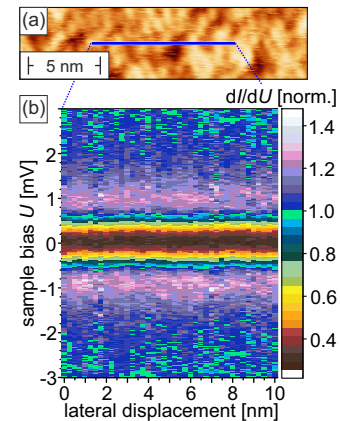


FIG. 6. (a) Topographic image of a TiNi_2Se_2 showing the “wormlike” structure. (b) Normalized dI/dU spectra measured along the 10-nm-long blue line marked in (a). No significant influence of the surface reconstruction on the width or shape of the superconducting gap is detected. Stabilization parameters are as follows: $U = -5$ mV, $I_{\text{set}} = 200$ pA, $U_{\text{mod}} = 0.1$ mV, $T = 1.2$ K.

We would like to state clearly already here, however, that in the case of cleaved $\text{TiNi}_2\text{Se}_2(001)$ surfaces we found the superconducting gap to be virtually independent of the particular local surface reconstruction. This is exemplarily shown in Fig. 6, which displays an image of the “wormlike” structure in (a) together with color-coded tunneling spectra in (b). No significant variation of the width or shape of the superconducting gap can be observed, even though the trajectory along which the STS data were measured crosses several corrugation minima and maxima of the surface reconstruction.

We believe that this finding is consistent with the structural data presented in Sec. III A. Our topographic STM data showed that the surface is dominated by $(\sqrt{2} \times \sqrt{2})R45^\circ$ and (2×1) reconstructions which are most likely the result of the polar character of $\text{TiNi}_2\text{Se}_2(001)$ planes. It appears that these reconstructions lead to the smallest possible distortion of the TiNi_2Se_2 bulk structure. Therefore, the superconducting properties measured on the $\text{TiNi}_2\text{Se}_2(001)$ surfaces closely resemble those of bulk-sensitive transport measurements.

3. Temperature dependence

Figure 7(a) shows temperature-dependent STS data. Starting from the lowest achievable temperature of $T = 1.2$ K (purple line), the gap width and depth decreases with increasing temperature until it completely vanishes at $T \gtrsim 3.2$ K (orange line). To analyze the temperature dependence of the superconducting gap in more detail the gap width was fitted by a simple BCS-like gap function [Eq. (1)]. Fits to the individual spectra for all temperatures shown in Fig. 7(a) can be inspected in the Supplemental Material, Fig. S2 [26]. The resulting gap size is plotted against the temperature in Fig. 7(b). It closely follows what is expected for a BCS-type gap (red line) [27],

$$\frac{1}{\eta(T_C)} = \int_0^{k_B T_D} \frac{\tanh \left[\frac{1}{2k_B T_C} \sqrt{\xi^2 + \Delta(T)^2} \right]}{\sqrt{\xi^2 + \Delta(T)^2}} d\xi, \quad (2)$$

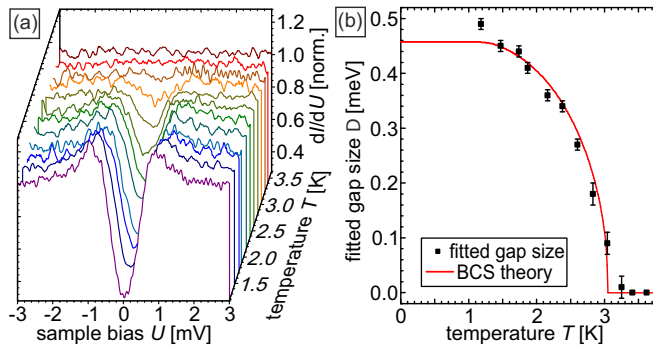


FIG. 7. (a) Temperature-dependent STS data of TiNi_2Se_2 . A pronounced superconducting gap is clearly visible at the lowest accessible temperature, $T = 1.2$ K (purple line). With increasing temperature the gap size is reduced and vanishes at about $T \gtrsim 3.2$ K (orange line). (b) Plot of the temperature-dependent gap size determined by fitting the STS data presented in (a) with Eq. (2) expected for a BCS-type superconductor (see main text for details). Stabilization parameters are as follows: $U = -5$ mV, $I_{\text{set}} = 200$ pA, $U_{\text{mod}} = 0.1$ mV.

with the Debye-temperature $T_D = 175$ and the interaction strength η which itself depends on T_C [7]. This temperature dependence of the gap was calculated numerically by using the BCS ratio $\Delta(0)/k_B T_c = 1.764$ [27], resulting in a critical temperature $T_c = 3.05$ K. Even though this T_c obtained from the fitting procedure is slightly lower than the one observed in transport measurements [7], the close correlation again suggests that superconductivity of TiNi_2Se_2 is driven by an s-wave pairing mechanism, similar to standard BCS-type superconductors.

4. Field dependence

To check the magnetic field dependence of superconducting TiNi_2Se_2 we experimentally investigated the impact of various magnetic fields up to 500 mT. Any spectrum was measured on the superconducting surface at maximal distance from neighboring vortex cores (see Fig. 9 below). Figure 8(a) shows the weakening of the superconducting gap with increasing strength of the field. Above 400 mT the gap vanishes completely. Sim-

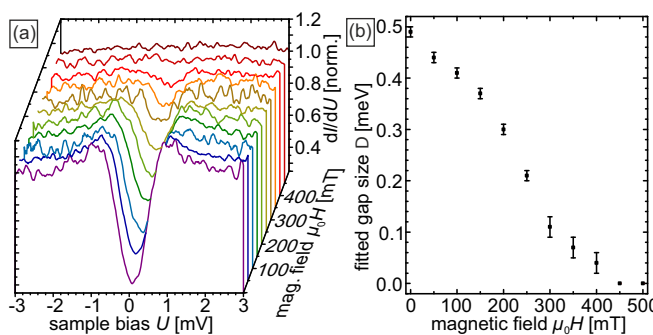


FIG. 8. (a) Magnetic field-dependent spectroscopy of TiNi_2Se_2 at $T = 1.2$ K. The gap becomes smaller with increasing magnetic field and vanishes for $B \gtrsim 400$ mT. Stabilization parameters are as follows: $U = -5$ mV, $I_{\text{set}} = 200$ pA, $U_{\text{mod}} = 0.1$ mV. (b) Plot of the field-dependent gap size determined by fitting the data in (a).

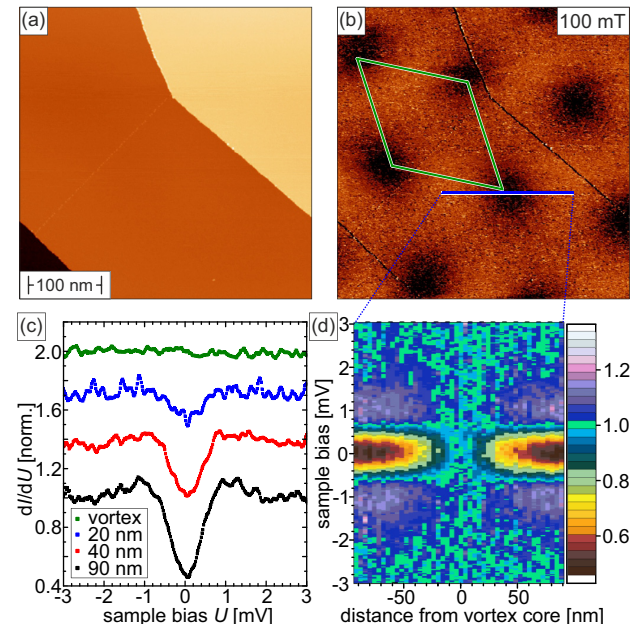


FIG. 9. (a) Topographic image of cleaved TiNi_2Se_2 . (b) Differential conductance maps of the same area as in (a) at a perpendicular magnetic field of 100 mT, showing the Abrikosov lattice. The unit cell of the vortex lattice as theoretically expected from Eq. (3) is indicated in green. The experimentally observed density of the vortices is in excellent agreement. (c) Some examples of scanning tunneling spectra measured directly at and at some selected distances from the vortex core. The superconducting gap is decreasing with decreasing distance to the vortex core where the gap vanishes completely. (d) Normalized dI/dU spectra as a function of their distance from the vortex core as measured along the 200-nm-long blue trajectory marked in (b). Scan parameters are as follows: $U = -1$ mV, $I_{\text{set}} = 50$ pA, $U_{\text{mod}} = 0.1$ mV, $T = 1.2$ K.

ilar to the above-mentioned temperature-dependent results, this value is again slightly lower than the results obtained in transport measurements [7]. Also these spectra were fitted by a BCS-like gap function. The individual fits for all magnetic fields up to 400 mT are shown in the Supplemental Material, Fig. S3 [26]. The resulting gap sizes are plotted in Fig. 8(b). The gap size decreases monotonously with magnetic field until the zero-bias conductance becomes undistinguishable from 1 at 450 mT. We conclude that the critical field is somewhere between $400 \text{ mT} < \mu_0 H_{c2} \leq 450 \text{ mT}$.

Obviously, both critical values (T_c and H_{c2}) are very close but slightly lower than the values acquired by transport measurements [7]. One possible explanation is that Cooper pairs in close proximity to the surface are slightly weaker bound than in the bulk, thereby weakening surface superconductivity. On the other hand our results indicate that the surface reconstruction discussed in Sec. III A of this article leads to no significant variations of the gap width, the conductance at the gap minimum, or the general spectral shape (see Fig. 6). This finding illustrates that superconductivity in TiNi_2Se_2 is dominated by bulk properties such that structural details and the resulting variation of the electronic structure can largely be ignored.

C. Abrikosov lattice

Type II superconductors undergo two transitions in a magnetic field. Whereas the whole magnetic field is expelled from the superconductor below the first critical value H_{c1} , magnetic flux quanta (vortices) run through the superconductor above H_{c1} until the superconducting state vanishes completely above the second critical field H_{c2} . In many cases these vortices form a dense-packed hexagonal lattice—the so-called Abrikosov lattice—which can be observed by STM, as shown for NbSe₂ by Hess and co-workers [28].

Figure 9(a) shows the topography of a 400 nm × 400 nm wide surface area of a cleaved TiNi₂Se₂ single crystal at a magnetic field of 100 mT. The surface area consists of three atomically flat terraces which are separated by two step edges with a height of ≈6.8 Å, in agreement with the above-mentioned $c/2$ distance [cf. Figs. 1(a) and 1(d)]. At the same location of the TiNi₂Se₂ surface we imaged the Abrikosov lattice by taking differential conductance dI/dU maps at a bias voltage of $U = -1$ mV, i.e., the onset of superconducting gap (cf. Fig. 5). It is shown in Fig. 9(b). One recognizes several roughly circularly shaped regions arranged in a hexagonal lattice where the dI/dU signal is reduced (dark). Their diameter amounts to about 60–70 nm. At these locations magnetic flux quanta run through the sample and destroy superconductivity. As indicated by a green rhombus in Fig. 9(b), the lattice parameter A of the Abrikosov lattice, which is given by

$$A = \frac{\Phi_0}{B}, \quad (3)$$

where $\Phi_0 = \frac{h}{2e}$ is a single flux quantum, matches the theoretically expected value very well.

Local spectroscopy data recorded directly at the vortex core and some selected distances show how the SC gap successively vanishes when approaching the vortex core [Fig. 9(c)]. Whereas the gap is clearly visible far away from the vortex (see black spectrum measured at a distance of about 90 nm), the gap intensity progressively decreases at shorter distances (red and blue spectra) until it completely vanishes directly at the vortex core (green spectrum). In contrast to similar measurements performed on NbSe₂ [28], where a pronounced zero-bias peak was observed in spectra taken in the center of the vortex, we observed no sign of a zero-bias anomaly on the TiNi₂Se₂ surface.

At the moment we can only speculate why the zero-bias conductance peak (ZBP) is absent. It is known that a ZBP in the vortex core is only observed in very pure samples. For example, for Ta-doped NbSe₂, Nb_(1-x)Ta_xSe₂ a vanishing of the ZBP was observed due to enhanced impurity scattering for Ta concentrations as low as a few percent only [29].

Even though our samples exhibit a Fermi liquid behavior with $\rho_{ab}(T) = \rho_0 + AT^2$, where $\rho_0 = 0.615 \mu\Omega \text{ cm}$ and $A = 4.94 \times 10^{-3} \mu\Omega \text{ cm/K}^2$ [7], and a residual resistivity ratio RRR = $\rho_{ab}(300 \text{ K})/\rho_{ab}(2 \text{ K}) \approx 103$, indicating a high quality of the single crystals, we cannot exclude that bulk crystalline defects are responsible for the absence of the ZBP. In fact, we find a mean free path $l = 17.3 \text{ nm}$ which is slightly shorter than the coherence length $\xi_{||} = 20.3 \text{ nm}$ [7], resulting in a ratio $(l/\xi_{||}) \approx 0.85$. In a systematic STS study of the vortex core spectra measured on Nb_(1-x)Ta_xSe₂ the transition from the clean (with ZBP) to the dirty limit (no ZBP) was found to occur at comparable $(l/\xi_{||})$ value [29]. This comparison suggests that for the TiNi₂Se₂(001) surface the absence of a ZBP is not related to the reconstructions present on the surface. It remains to be studied whether the relatively high degree of disorder of the reconstruction present on the surface leads to a further reduction of the quasiparticle lifetime.

IV. CONCLUSION

In conclusion, we analyzed the structural and electronic properties of the Ni-based heavy-electron superconductor TiNi₂Se₂. Depending on the cleavage temperature and the measurement conditions the surface shows different reconstructions in STM experiments which all satisfy the condition of surface charge density of $\rho < 0.5 e^-$ per unit cell required to avoid a polar catastrophe due to the polar character of the TiNi₂Se₂(001) planes. While for low-temperature cleavage a $\sqrt{2} \times \sqrt{2}$ reconstruction shows up, warming induces a transformation into a (2 × 1) structure and eventually at $T \geq 126 \text{ K}$ results in the more irregular “wormlike” structure. Analyzing the electronic properties, we found a superconducting transition with critical values of $T_c = 3.05 \text{ K}$ and $\mu_0 H_{c2} = 0.45 \text{ T}$, i.e., very close to the corresponding bulk values. At small magnetic fields we observed the formation of vortices which are arranged in a hexagonal Abrikosov lattice. Local tunneling spectra taken within the vortex core show a vanishing superconducting gap but also reveal the absence of any zero-bias anomaly. Together with the shape of the tunneling spectra this observation points to an *s*-wave pairing mechanism with an isotropic gap, in agreement with the transport measurements [7,8].

ACKNOWLEDGMENTS

The experimental work was supported by DFG (through SFB 1170 “ToCoTronics”; Project No. A02). Work at ZJU was supported by the National Basic Research Program of China (Grants No. 2016FYA0300402 and No. 2015CB921004), the National Science Foundation of China (Grant No. 11374261), and the Fundamental Research Funds for the Central University of China.

-
- [1] J. G. Bednorz and K. A. Müller, *Z. Phys. B* **64**, 189 (1986).
 - [2] Y. Kamihara, H. Hiramatsu, M. Hirano, R. Kawamura, H. Yanagi, T. Kamiya, and H. Hosono, *J. Amer. Chem. Soc.* **128**, 10012 (2006).
 - [3] Y. Kamihara, T. Watanabe, M. Hirano, and H. Hosono, *J. Amer. Chem. Soc.* **130**, 3296 (2008).
 - [4] R. Zhi-An, L. Wei, Y. Jie, Y. Wei, S. Xiao-Li, Zheng-Cai, C. Guang-Can, D. Xiao-Li, S. Li-Ling, Z. Fang, and Z. Zhong-Xian, *Chin. Phys. Lett.* **25**, 2215 (2008).
 - [5] P. J. Hirschfeld, M. M. Korshunov, and I. I. Mazin, *Rep. Prog. Phys.* **74**, 124508 (2011).
 - [6] M. Kenzelmann, T. Strässle, C. Niedermayer, M. Sigrist, B. Padmanabhan, M. Zolliker, A. D. Bianchi, R. Movshovich,

- E. D. Bauer, J. L. Sarrao, and J. D. Thompson, *Science* **321**, 1652 (2008).
- [7] H. Wang, C. Dong, Q. Mao, R. Khan, X. Zhou, C. Li, B. Chen, J. Yang, Q. Su, and M. Fang, *Phys. Rev. Lett.* **111**, 207001 (2013).
- [8] X. C. Hong, Z. Zhang, S. Y. Zhou, J. Pan, Y. Xu, H. Wang, Q. Mao, M. Fang, J. K. Dong, and S. Y. Li, *Phys. Rev. B* **90**, 060504 (2014).
- [9] H. Wang, Q. Mao, H. Chen, Q. Su, C. Dong, R. Khan, J. Yang, B. Chen, and M. Fang, *J. Phys.: Condens. Matter* **27**, 395701 (2015).
- [10] N. Xu, C. E. Matt, P. Richard, A. van Roekeghem, S. Biermann, X. Shi, S.-F. Wu, H. W. Liu, D. Chen, T. Qian, N. C. Plumb, M. Radović, H. Wang, Q. Mao, J. Du, M. Fang, J. Mesot, H. Ding, and M. Shi, *Phys. Rev. B* **92**, 081116 (2015).
- [11] H. Chen, J. Yang, C. Cao, L. Li, Q. Su, B. Chen, H. Wang, Q. Mao, B. Xu, J. Du, and M. Fang, *Supercond. Sci. Technol.* **29**, 045008 (2016).
- [12] J. R. Neilson, A. Llobet, A. V. Stier, L. Wu, J. Wen, J. Tao, Y. Zhu, Z. B. Tesanovic, N. P. Armitage, and T. M. McQueen, *Phys. Rev. B* **86**, 054512 (2012).
- [13] J. R. Neilson, T. M. McQueen, A. Llobet, J. Wen, and M. R. Suchomel, *Phys. Rev. B* **87**, 045124 (2013).
- [14] M. C. Boyer, K. Chatterjee, W. D. Wise, G. F. Chen, J. L. Luo, N. L. Wang, and E. W. Hudson, [arXiv:0806.4400](https://arxiv.org/abs/0806.4400).
- [15] Y. Yin, M. Zech, T. L. Williams, X. F. Wang, G. Wu, X. H. Chen, and J. E. Hoffman, *Phys. Rev. Lett.* **102**, 097002 (2009).
- [16] F. Massee, S. de Jong, Y. Huang, J. Kaas, E. van Heumen, J. B. Goedkoop, and M. S. Golden, *Phys. Rev. B* **80**, 140507 (2009).
- [17] M. Gao, F. Ma, Z.-Y. Lu, and T. Xiang, *Phys. Rev. B* **81**, 193409 (2010).
- [18] H. Zhang, J. Dai, Y. Zhang, D. Qu, H. Ji, G. Wu, X. F. Wang, X. H. Chen, B. Wang, C. Zeng, J. Yang, and J. G. Hou, *Phys. Rev. B* **81**, 104520 (2010).
- [19] M. Dreyer, M. Gubrud, S. Saha, N. P. Butch, K. Kirshenbaum, and J. Paglione, *J. Phys.: Condens. Matter* **23**, 265702 (2011).
- [20] J. E. Hoffman, *Rep. Prog. Phys.* **74**, 124513 (2011).
- [21] N. Nakagawa, H. Y. Hwang, and D. A. Muller, *Nat. Mater.* **5**, 204 (2006).
- [22] V. B. Nascimento, A. Li, D. R. Jayasundara, Y. Xuan, J. O’Neal, S. Pan, T. Y. Chien, B. Hu, X. B. He, G. Li, A. S. Sefat, M. A. McGuire, B. C. Sales, D. Mandrus, M. H. Pan, J. Zhang, R. Jin, and E. W. Plummer, *Phys. Rev. Lett.* **103**, 076104 (2009).
- [23] F. C. Niestemski, V. B. Nascimento, B. Hu, E. W. Plummer, J. Gillett, S. Sebastian, Z. Wang, and V. Madhavan, [arXiv:0906.2761](https://arxiv.org/abs/0906.2761).
- [24] J. Tersoff and D. R. Hamann, *Phys. Rev. B* **31**, 805 (1985).
- [25] R. C. Dynes, V. Narayanamurti, and J. P. Gorno, *Phys. Rev. Lett.* **41**, 1509 (1978).
- [26] See Supplemental Material at <http://link.aps.org/supplemental/10.1103/PhysRevB.97.014514> for details regarding fits to superconducting tunneling spectra and temperature- and field-dependent spectra, which includes Refs. [30–32].
- [27] M. Tinkham, *Introduction to Superconductivity*, 2nd ed. (Dover Publications, Mineola, 1996).
- [28] H. F. Hess, R. B. Robinson, R. C. Dynes, J. M. Valles, and J. V. Waszczak, *Phys. Rev. Lett.* **62**, 214 (1989).
- [29] C. Renner, A. D. Kent, P. Niedermann, O. Fischer, and F. Lévy, *Phys. Rev. Lett.* **67**, 1650 (1991).
- [30] S.-H. Ji, T. Zhang, Y.-S. Fu, X. Chen, X.-C. Ma, J. Li, W.-H. Duan, J.-F. Jia, and Q.-K. Xue, *Phys. Rev. Lett.* **100**, 226801 (2008).
- [31] M. Ruby, B. W. Heinrich, J. I. Pascual, and K. J. Franke, *Phys. Rev. Lett.* **114**, 157001 (2015).
- [32] M. Ternes, W.-D. Schneider, J.-C. Cuevas, C. P. Lutz, C. F. Hirjibehedin, and A. J. Heinrich, *Phys. Rev. B* **74**, 132501 (2006).